

Wave-Induced Motion and Drag Reduction of Kelp

Jayde F. Meng¹, Marcelo Chamecki¹

¹Department of Atmospheric and Oceanic Sciences, University of California, Los Angeles, CA 90025, USA

Key Points:

- A 2D parameter space is proposed to characterize dominant forces and classify different types of kelp motion
- Inertial forces can significantly impact frond motion and drag reduction, and even lead to drag augmentation (compared to rigid fronds)
- We provide empirical fits to quantify drag reduction/augmentation in low- and high-inertia conditions

Corresponding author: Marcelo Chamecki, chamecki@ucla.edu

Abstract

It is well known that the motion of flexible vegetation leads to drag reduction in comparison to rigid vegetation. In this study, we use a numerical model to investigate how the detailed motion of kelp fronds in response to forcing by surface gravity waves can impact the drag exerted by the kelp on waves. We find that this motion can be characterized in terms of three dimensionless numbers: (1) the ratio of hydrodynamic drag to buoyancy, (2) the ratio of blade length to wave excursion, and (3) the Keulegan-Carpenter number, which measures the ratio of drag to inertial forces. We quantify drag reduction, and find that inertial forces can significantly impact the amplitude of kelp motion and amount of kelp drag reduction. Under certain wave conditions, inertial forces can cause kelp fronds to accelerate more quickly relative to the wave, which can lead to increased drag reduction and reduced wave energy dissipation. In some conditions, frond motion leads to drag augmentation in comparison to rigid fronds. Additionally, we discuss other features of kelp motion, such as the degree of asymmetry, and their relationship with enhanced drag reduction.

Plain Language Summary

We use a numerical model to study how kelp fronds move in response to passing ocean waves. Flexible motion reduces the drag forces experienced by the kelp and increases survival in extreme conditions such as energetic waves. Frond motion also reduces the amount of wave energy dissipation. The type of motion that the fronds undergo in response to different types of waves is determined by the dominant forces, and so is the amount of drag reduction. Our findings show that, unlike other types of aquatic vegetation, inertial forces (e.g. due to the pressure variations in the water) can be as important as (and sometimes more important) than the drag forces caused by the flow.

1 Introduction

Macroalgae species, such as kelp, are integral to the health of many coastal ecosystems. Kelp forests help preserve biodiversity by serving as habitats and food sources for different marine species (Dayton et al., 1984; Schiel & Foster, 2015). Kelp forests also help remediate anthropogenic changes, by mitigating eutrophication pollution through nitrate removal (Gao et al., 2021) and reducing ocean acidification and offsetting carbon dioxide emissions via carbon sequestration (Froehlich et al., 2019; Hoegh-Guldberg et al., 2019). Globally, kelp forests generate an average of \$500 billion a year in terms of ecosystem services (Eger et al., 2023).

41 Moreover, kelp harvesting is central to numerous local economies. Many cultures around
42 the world have a rich history of relying on kelp as a food source, a way to enhance fisheries, a fer-
43 tilizer for soil, etc. (Thornton, 2015; Kain & Dawes, 1987). More recently, alginate sourced from
44 kelp has also been utilized as an important additive in pharmaceutical and biomedical industries
45 (Peteiro, 2018). Furthermore, the high energy content and fast growth rates of kelp have singled
46 them out to be a potential source of biofuel that does not compete for space with land-grown crops
47 for the food industry (Milledge et al., 2014; Frieder et al., 2022).

48 With all of these benefits, it is critical to understand how we can sustainably support the
49 growth and maintenance of kelp forests and farms. In particular, we are interested in the hydro-
50 dynamic interactions between kelp and ocean waves. This study focuses primarily on the hydro-
51 dynamics of the kelp species *Macrocystis pyrifera*, more commonly known as giant kelp. Giant
52 kelp is native to the coasts of California and is particularly well-suited for the purposes of farm-
53 ing due to its fast growth rates (up to 0.5 meters per day). They are the largest species of algae
54 and can reach lengths of 20 meters or more (Abbott & Hollenberg, 1992).

55 This type of kelp is made up of dozens of fronds attached to a holdfast, which keeps the
56 kelp anchored to the substrate. Each frond consists of a stem-like stipe and leaf-like blades, and
57 at the base of each blade is a pneumatocyst, or a gas-filled bladder. These pneumatocysts allow
58 *M. pyrifera* to be highly buoyant. Giant kelp stipes also have relatively low rigidity compared to
59 seagrasses, allowing stipes to easily bend in response to hydrodynamic forces. A diagram of kelp
60 physiology is given in Fig. 1(a).

61 Many past observational studies on *M. pyrifera* (henceforth simply referred to as kelp) hy-
62 drodynamics have focused on quantifying the bulk effects of kelp on the flow. The drag force im-
63 parted by the kelp on the currents reduces flow rates through kelp forests (Jackson & Winant, 1983;
64 Gaylord et al., 2007). For example, Monismith et al. (2022) estimated the scaling for kelp for-
65 est drag coefficient in tidal flows via biomass relationships. Laboratory studies have also shown
66 that the presence of kelp modifies wave orbital velocities (Rosman et al., 2013). However, kelp
67 forests generally dissipate minimum amounts of wave energy due to its highly flexible nature (Elwany
68 et al., 1995).

69 Because of its nearshore environment, kelp are especially sensitive to the forces caused by
70 surface gravity waves (Gaylord et al., 2003). High energy wave amplitudes can cause kelp stipes
71 to break and entangle, or even dislodge fronds from their holdfast (Seymour et al., 1989; Day-
72 ton et al., 1984). Kelp fronds have also been observed to respond differently to waves with dif-

73 ferent periods (Mullarney & Pilditch, 2017). Generally, flexibility is a strategy employed by sea-
74 grasses and algae to reduce drag forces and increase survivability in high-flow environments (Vogel,
75 1984; Utter & Denny, 1996). In return, the drag exerted on the waves by kelp is highly depen-
76 dent on the detailed motion of the kelp frond. Thus, the two-way interaction between flexible kelp
77 fronds and waves impact both, the survivability of kelp and the physical properties of the waves.

78 Numerical models have also been used to predict the forces that individual kelp fronds un-
79 dergo in different wave conditions, and thus, how likely they are to survive. For example, Jackson
80 and Winant (1983) modeled kelp stipes as rigid vertical columns, while Utter and Denny (1996)
81 represented kelp fronds as buoys attached to a flexible rope and predicted kelp survivability rates
82 under different wave conditions. They model a single point element where hydrodynamic forces
83 such as buoyancy, drag, and pressure gradient forces are countered by tension (Utter & Denny,
84 1996; Denny et al., 1997).

85 Additionally, a number of more sophisticated numerical models have been developed to
86 investigate submerged aquatic vegetation motion under wave conditions, including but not lim-
87 ited to variations of the Euler-Bernoulli beam model utilized by Marjoribanks et al. (2014), Zeller
88 et al. (2014), and Luhar and Nepf (2016). Zhu et al. (2020) expanded on this work and developed
89 a consistent-mass cable model to study asymmetric motion of aquatic vegetation. However, these
90 models have not been applied to the study of giant kelp, in part because they suffer from numer-
91 ical stability issues in cases with low bending stiffness (Zeller et al., 2014).

92 A major thrust of theoretical and numerical studies is to develop understanding and quan-
93 tification of how plant motion affects drag reduction. For instance, Luhar and Nepf (2011) de-
94 veloped a scaling model for the drag of smaller seagrasses in currents by considering the differ-
95 ent balances between drag, buoyancy, and rigidity. Luhar and Nepf (2016) and Lei and Nepf (2019)
96 extended this work to wave conditions and the meadow scale, mainly focusing on seagrasses for
97 which hydrodynamic forcing is primarily balanced by blade stiffness. Henderson (2019) com-
98 plemented this work by also analyzing drag reduction in plants where drag forces are balanced
99 by both stiffness and buoyancy.

100 Notably, most of the past work has been conducted with the assumption of drag dominated
101 flows; that is, inertial forces such as the pressure gradient and added mass forces are insignifi-
102 cant when compared to drag forces and do not contribute much to plant motion. This is relatively
103 accurate for smaller seagrass species, which usually grow in very shallow waters. However, kelp
104 often grows in deeper waters and fronds can be quite long. Furthermore, typical wave conditions

105 of coastal California create a natural environment where inertial forces become important. To-
 106 gether, all of these factors (longer plant lengths, the importance of inertial forces, the predom-
 107 inance of buoyancy over bending stiffness as a restoring force) produce distinct dynamical be-
 108 havior and lead to different laws of drag reduction.

109 Thus, the purpose of this study is to gain a better understanding of kelp hydrodynamics by
 110 investigating the impact of inertial forces on kelp motion and consequently, kelp drag reduction.
 111 We first develop a generalized numerical model for kelp frond motion, and the model is then used
 112 to study the response of kelp fronds to different wave conditions observed on the coast of Cal-
 113 ifornia. We focus specifically on the importance of inertial forces and how that impacts differ-
 114 ent aspects of frond motion and drag reduction.

115 2 Methods

116 2.1 Model Description

117 We constructed a two dimensional model for the motion of an individual kelp frond fol-
 118 lowing the approach outlined by Rosman et al. (2013) and Marjoribanks et al. (2014), which can
 119 be considered as a refinement of the simple tethered-buoy model developed by Utter and Denny
 120 (1996). The kelp frond is discretized into n segments, and each segment is modeled as a point
 121 mass attached to a string with the flexibility and tensile stiffness of kelp stipes. Thus, the kelp frond
 122 is modeled as a set of point masses connected by strings. The position of each point mass is rep-
 123 resented by the vector $\mathbf{x}_i = (x_i, z_i)$, and its velocity by the vector $d\mathbf{x}_i/dt$. A visualization of this
 124 representation is given in Fig. 1(b). Note that kelp usually grows to form a dense canopy float-
 125 ing on the surface that can significantly enhance the total drag (Rosman et al., 2013). For sim-
 126 plicity, we do not consider the presence of the surface canopy here, and focus only on situations
 127 in which the frond length is smaller than the water depth.

128 The motion of each point mass is governed by Newton’s second law. Following Utter and
 129 Denny (1996), Denny et al. (1997), and Rosman et al. (2013), we use Morison’s equation (e.g.,
 130 see Journee & Massie, 2000) to describe the forces acting on kelp. In the present model, we in-
 131 cluded the five main forces that determine kelp motion: buoyancy, drag, added mass, pressure
 132 gradient, and tension. We assume that the drag is exerted by the area of the blades, the bending
 133 stiffness originates from the kelp stipe, and the buoyancy comes from the pneumatocysts. Be-
 134 cause kelp stipes are very flexible, we assume that their rigidity, or resistance to bending, is neg-
 135 ligible. As in Utter and Denny (1996), we also neglect lift and skin friction forces, which are rel-

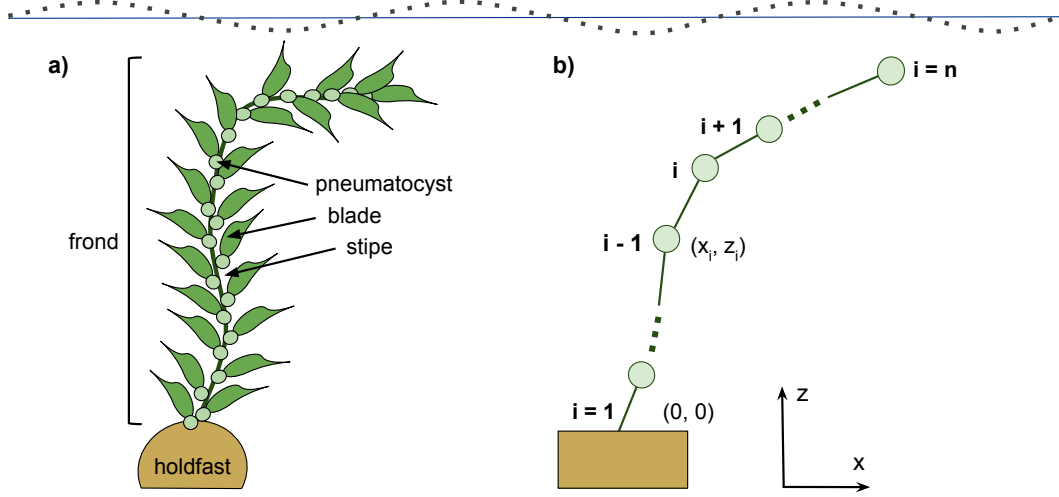


Figure 1. (a) *M. pyrifera* frond and (b) schematic of the discretization of the frond in the numerical model.

136 actively inconsequential. Assuming each segment has an effective mass m_k , the governing equa-
 137 tion of motion for the i^{th} segment is given by

$$138 \quad m_k \frac{d^2 \mathbf{x}_i}{dt^2} = \mathbf{F}_{D,i} + \mathbf{F}_{B,i} + \mathbf{F}_{P,i} + \mathbf{F}_{AM,i} + \mathbf{F}_{T,i} + \mathbf{F}_{T,i+1}, \quad (1)$$

139 where $\mathbf{F}_{D,i}$ is the drag force, $\mathbf{F}_{B,i}$ is the buoyant force, $\mathbf{F}_{P,i}$ is the pressure gradient force, $\mathbf{F}_{AM,i}$
 140 is the added mass force, and $\mathbf{F}_{T,i}$ and $\mathbf{F}_{T,i+1}$ are the tension forces on the strings that connect the
 141 point mass to its neighboring masses.

142 The drag force is modeled using a quadratic equation given in terms of relative velocity

$$143 \quad \mathbf{F}_{D,i} = \frac{1}{2} \rho_w C_d A_i \left| \mathbf{u}_i - \frac{d\mathbf{x}_i}{dt} \right| \left(\mathbf{u}_i - \frac{d\mathbf{x}_i}{dt} \right), \quad (2)$$

144 where ρ_w is the density of seawater, C_d is the drag coefficient, A_i is the maximal projected area
 145 of each frond segment, and $\mathbf{u}_i = (u_{x,i}, u_{z,i})$ is the two-dimensional fluid velocity vector. Con-
 146 trary to most models of seagrass dynamics (Luhar & Nepf, 2011, 2016), we assume that there
 147 is no reduction in exposed area with bending. This is because as kelp fronds bend, their blades
 148 remain oriented with the flow, so the exposed area changes very little (e.g., the contribution of
 149 the area of the stipe to the drag force is negligible).

150 The buoyancy force is given by

$$151 \quad \mathbf{F}_{B,i} = (\rho_k - \rho_w) V_i \mathbf{g}, \quad (3)$$

152 where ρ_k is the density of the kelp frond, V_i is the volume of each segment, and \mathbf{g} is the gravi-
 153 tational acceleration vector.

154 Two forces are associated with the acceleration of the fluid: the pressure gradient force (or
155 Froude-Krylov force) and the added mass force. They are given, respectively, by

$$156 \quad \mathbf{F}_{P,i} = \rho_w V_i \frac{\partial \mathbf{u}_i}{\partial t} \quad (4)$$

157 and

$$158 \quad \mathbf{F}_{AM,i} = C_a \rho_w V_i \left(\frac{\partial \mathbf{u}_i}{\partial t} - \frac{d^2 \mathbf{x}_i}{dt} \right), \quad (5)$$

159 where C_a is the added mass coefficient. We will refer to these two forces as the inertial forces
160 acting on the kelp frond.

161 In oscillatory flows, it is typical to model the drag and added mass coefficients (C_d and C_a)
162 as a function of the Keulegan-Carpenter number (KC), which characterizes the ratio between in-
163 ertial and drag forces (e.g., see Luhar & Nepf, 2016). This is done based on experiments with
164 flat plates and similar objects in oscillatory flow (Keulegan & Carpenter, 1956; Sarpkaya & O’Keefe,
165 1996), for which $KC = U_w T_p / d$, where U_w is a characteristic velocity scale, T_p is the wave pe-
166 riod, and d is the thickness of the plate. These effects are attributed to the vortex shedding from
167 these blunt objects and there is little reason to believe that kelp fronds have a similar behavior.
168 Therefore, we do not include explicit effects of KC on C_d and C_a in our model.

169 Each point mass is also subject to tension forces from the string connected to the point mass
170 below, $\mathbf{F}_{T,i}$, and to the point mass above, $\mathbf{F}_{T,i+1}$. Thus, the total tension force on each segment
171 is given by the sum of the two tensions, or

$$172 \quad \mathbf{F}_{T,i} + \mathbf{F}_{T,i+1} = -EA_c \frac{|\mathbf{x}_i - \mathbf{x}_{i-1}| - l_i}{l_i} \mathbf{e}_{s,i} + EA_c \frac{|\mathbf{x}_{i+1} - \mathbf{x}_i| - l_{i+1}}{l_{i+1}} \mathbf{e}_{s,i+1}, \quad (6)$$

173 when $|\mathbf{x}_i - \mathbf{x}_{i-1}| > l_i$ and $|\mathbf{x}_{i+1} - \mathbf{x}_i| > l_{i+1}$, where l_i and l_{i+1} are the lengths of each segment.
174 Here we have adopted the elastic model used by Utter and Denny (1996) to represent the tension
175 on the string, and E is the modulus of elasticity of the kelp, while $\mathbf{e}_{s,i}$ and $\mathbf{e}_{s,i+1}$ are the unit vec-
176 tors in the direction of their respective segments. We assume that $\mathbf{F}_{T,i} = 0$ at the tip of the frond
177 (last segment, $i = n$), and that the plant is rooted at $\mathbf{x}_0 = (0, 0)$. Note that by adopting this model
178 and solving for the tension force explicitly, our model allows for stretching and compression of
179 each frond segment.

180 The complete equation after dividing all terms by the total volume occupied by each kelp
181 segment is

$$182 \quad (\rho_k + C_a \rho_w) \frac{d^2 \mathbf{x}_i}{dt} = \frac{1}{2} \rho_w C_d \frac{A_i}{V_i} \left| \mathbf{u}_i - \frac{d\mathbf{x}_i}{dt} \right| \left(\mathbf{u}_i - \frac{d\mathbf{x}_i}{dt} \right) + (\rho_k - \rho_w) \mathbf{g} + (\rho_w + C_a \rho_w) \frac{\partial \mathbf{u}_i}{\partial t} \\ 183 \quad + \frac{EA_c}{V_i} \left(-\frac{|\mathbf{x}_i - \mathbf{x}_{i-1}| - l_i}{l_i} \mathbf{e}_{s,i} + \frac{|\mathbf{x}_{i+1} - \mathbf{x}_i| - l_{i+1}}{l_{i+1}} \mathbf{e}_{s,i+1} \right) \quad (7)$$

184 where the effective mass m_k is given by $V_i(\rho_k + C_a \rho_w)$. The set of equations (7) is numerically
 185 integrated in time using a fourth-order Runge-Kutta algorithm to solve for the position of all point
 186 masses $\mathbf{x}_i = (x_i, z_i)$ and associated velocities. In our current model implementation, all the seg-
 187 ment have the same geometrical properties such that A_i , l_i , and V_i are all constant for all i .

188 The main differences between our modeling approach and the more standard models used
 189 for seagrass (e.g., Marjoribanks et al., 2014; Zeller et al., 2014; Luhar & Nepf, 2016) are that:
 190 (1) we neglect bending stiffness given that the restoring force to resist motion in kelp is mostly
 191 provided by the buoyancy force, and models that include bending stiffness for low stiffness sys-
 192 tems generate numerical instability issues such as poor convergence (Zeller et al., 2014); (2) we
 193 allow for elastic stretching deformation instead of imposing a constant frond length, which is im-
 194 portant in modeling kelp motion (Johnson & Koehl, 1994; Utter & Denny, 1996). As an aside,
 195 we attempted to use the model developed by (Luhar & Nepf, 2016) to simulate some of our cases,
 196 but ran into numerical instability issues even for the shortest fronds under the least energetic wave
 197 conditions despite using a very fine grid resolution and small time step.

198 2.2 Model Setup

199 We study frond motion by imposing a two-dimensional linear wave flow field represented
 200 by $\mathbf{u} = (u_x, u_z)$. For a coordinate system located at the bottom of the ocean, the wave orbital
 201 velocity components at a location (x, z) are given by (Dean & Dalrymple, 1991):

$$202 \begin{cases} u_x = A_w \omega \frac{\cosh(kz)}{\sinh(kH)} \cos(kx - \omega t) \\ u_z = A_w \omega \frac{\sinh(kz)}{\sinh(kH)} \sin(kx - \omega t) \end{cases} \quad (8)$$

203 where A_w is the wave amplitude, ω is the wave frequency, k is the wavenumber, and $H = 12$
 204 m is the depth of the water column (note that in this coordinate system, $z = H$ at the surface).

205 To investigate the motion of kelp in its natural habitat, we utilized buoy data from the Coastal
 206 Data Information Program (CDIP; <https://cdip.ucsd.edu>). More specifically, buoys 87, 88,
 207 and 89 recorded local wave conditions in real kelp forests along the coast of the Channel Islands
 208 (Santa Rosa and Santa Cruz Islands) from October 1995 through December 1995. We used their
 209 measurements of significant wave height, H_s , and peak wave period, T_p , to determine typical wave
 210 conditions within natural kelp forests on the California coast. The joint probability density func-
 211 tion of measured significant wave height and wave period is shown in Fig. 2. In total, we selected
 212 sixteen different wave conditions covering the full realistic range of observed waves. For the sim-
 213 ple monochromatic wave model, we approximated the wave amplitude as $A_w = H_s/2$ and cal-

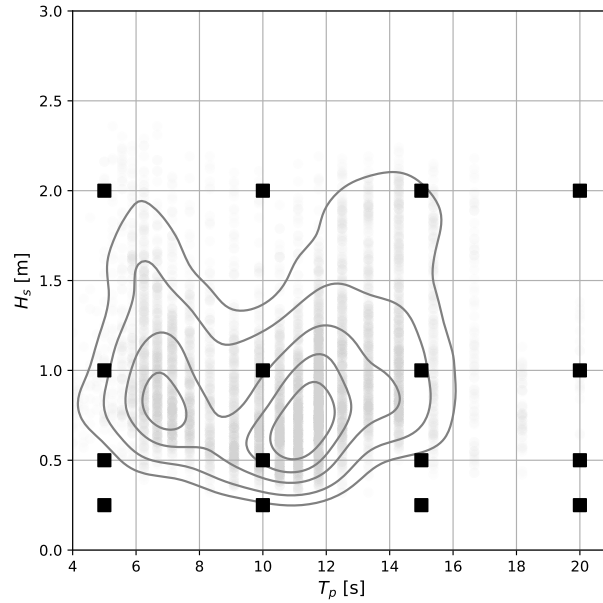


Figure 2. Simulated wave conditions. Light gray circles represent the aggregated CDIP measurements, and the gray lines represent the probability density function of the data (levels: 0.1, 0.25, 0.5, 0.75, 0.9). Black squares represent the conditions we selected for our runs. Data from CDIP, Scripps Institution of Oceanography.

214 culated the wave frequency from $\omega = 2\pi/T_p$ and the wave number from the dispersion relation
 215 $\omega = \sqrt{gk \tanh(kH)}$. The resulting waves fall in the range of $1/3 < kH < 2$, so we avoid us-
 216 ing approximations for deep-water or shallow-water waves.

217 The kelp properties used in the model were mostly compiled from Utter and Denny (1996),
 218 and these values are presented in Table 1. Here, the kelp density ρ_k is supposed to represent the
 219 bulk density of the frond, including the gas-filled pneumatocysts. The value adopted here was
 220 obtained from Rosman et al. (2013) and was confirmed from measurements of frond mass and
 221 volume (K. A. Davis unpubl.). Notably, this is about 40% larger than the value adopted by Henderson
 222 (2019). The drag coefficient adopted here is from the intercept of the drag-velocity plot by Utter
 223 and Denny (1996) (i.e., the drag for a rigid frond), and it is in good agreement with the mode of
 224 the distribution obtained by Monismith et al. (2022) for intermediate biomass kelp forests. Fi-
 225 nally, we obtained an estimate of frond volume indirectly from the frond projected area, the av-
 226 erage mass per unit area, and the frond density.

Table 1. List of kelp properties and their associated variables and values. All values are from (Utter & Denny, 1996), except for ρ_k which is taken from (Rosman et al., 2013).

Variable	Description	Value
ρ_k	Density of kelp	850 [kg m ⁻³]
ρ_w	Density of seawater	1025 [kg m ⁻³]
C_a	Added mass coefficient	3
C_d	Drag coefficient	0.0148
l	Fronde length	2, 5, 10 [m]
A	Maximal projected area of a frond	$0.297 \times l^{0.955}$ [m ²]
A_c	Cross-sectional area of a stipe	4.1×10^{-5} [m ²]
M_A	Average mass per unit area	0.774 [kg m ²]
V	Estimated volume of frond	$V = \frac{M_A A}{\rho_k}$ [m ³]
E	Modulus of elasticity	1.91×10^7 [Pa]

227 For each of the sixteen wave parameters, we tested three different frond lengths: 2 m, 5 m,
 228 and 10 m. Because kelp fronds can grow to be quite large, these lengths were selected in order
 229 to illustrate how kelp behaves in different wave conditions over its entire life cycle. This com-
 230 bination of plant length and wave conditions resulted in 48 simulations (see Table 2). Out of these
 231 cases, there were two that showed unrealistic amounts of stretching and compression (i.e. larger
 232 than 1% of the frond length) due to the elasticity of the kelp stipe: (1) $l = 10$ m, $H_s = 1$ m,
 233 $T_p = 5$ s; (2) $l = 10$ m, $H_s = 2$ m, $T_p = 5$ s. Thus, we removed these two cases from further
 234 analysis. The wave conditions in the removed cases are exceptionally high energy, and rarely oc-
 235 cur in the real world (see Fig. 2). We postulate that realistically, kelp fronds would probably be-
 236 come dislodged in those extreme, storm like wave conditions.

237 Each model kelp frond is discretized into 50 nodes, and initially starts at rest in a vertically
 238 upright position. To maximize accuracy while preserving stability, we set a time step of $\Delta t =$
 239 $T_p/10000$. We found that generally, the model kelp fronds required 5-7 wave periods before reach-
 240 ing an equilibrium cycle. Thus, we ran each simulation for 10 wave cycles, and only data from
 241 the last wave cycle were utilized for analysis. Tests showed no sensitivity of the results to using
 242 more nodes or reducing the time step.

243 It is rather difficult to perform validation of our code, as most detailed data from flume ex-
 244 periments available (e.g. Zeller et al., 2014; Luhar & Nepf, 2016) is for systems in which the bend-

ing stiffness is important. Therefore, we validate the model and test the assumption that stiffness
 is not important against the theory for steady flow developed by Luhar and Nepf (2011), and present
 results for the range of kelp and wave properties relevant to our study in Appendix A.

2.3 Theory

Luhar and Nepf (2016) first introduced three dimensionless parameters that govern blade
 motion in wave conditions: the Cauchy number (Ca), buoyancy parameter (B), and the ratio of
 blade length to wave excursion (L). These parameters are given by

$$Ca = \frac{\frac{1}{2}\rho_w C_d A U_w^2}{\frac{EI}{l^2}} \quad (9)$$

$$B = \frac{(\rho_w - \rho_k)gV}{\frac{EI}{l^2}} \quad (10)$$

$$L = \frac{l\omega}{U_w} = \frac{l}{\Delta x_w} \quad (11)$$

Note that quantities denoted without the subscript i refer to the same variable for the entire frond
 instead of per segment (e.g., A_i is the projected frond area for each segment in the numerical model,
 while A is the projected area for the entire frond).

The Cauchy number Ca represents the ratio of drag forces (the most common force driv-
 ing plant motion) to restoring force due to stiffness, while B represents the ratio of buoyancy to
 stiffness (i.e., the two forces that act to reduce plant motion). The parameter L also impacts blade
 dynamics, as is discussed below. Here, I is the second moment of area (for kelp stipes with cir-
 cular cross-sectional area, $I = \pi r_s^4/4$, where r_s is the radius of the stipe), and U_w and Δx_w
 are characteristic scales for the horizontal wave orbital velocities and excursions, respectively. Be-
 cause kelp fronds are typically much longer and grow in deeper water than seagrasses, the vari-
 ation of the wave orbital velocity along the length of the frond can be important. We define U_w
 as the amplitude of the horizontal wave orbital velocity averaged over the length of the frond

$$U_w = \frac{1}{l} \int_0^l A_w \omega \frac{\cosh(kz)}{\sinh(kH)} dz = \frac{A_w \omega}{kl} \frac{\sinh(kl)}{\sinh(kH)}. \quad (12)$$

Consequently, we also define Δx_w as an average along the length, or $\Delta x_w = U_w/\omega$. In this way,
 L is interpreted as the ratio between frond length and average horizontal wave excursion. Note
 that as a result of our definition of U_w , any parameter that is function of U_w implicitly takes into
 account the impact of wave decay with depth.

In most seagrasses, drag is the main force driving motion, bending stiffness is the main restor-
 ing mechanism, buoyancy is negligible, and blade dynamics and drag reduction can be fully char-
 acterized by Ca and L . In steady flow, for $Ca \ll 1$, the blade remains upright and has very lit-

272 the drag reduction (Luhar & Nepf, 2011). For $Ca \gg 1$, significant bending occurs before the
 273 restoring force balances the drag force and this reconfiguration allows for a large drag reduction
 274 (via reduction in the plant surface area). In unsteady flows, drag reduction in the $Ca \gg 1$ limit
 275 also depends on the excursion of the blade, which Luhar and Nepf (2016) quantified using L . When
 276 $L \ll 1$, the blade length is much smaller than the wave excursion, so the blade should reach a
 277 maximum excursion while the fluid continues traveling past it. Thus, the blade behaves similarly
 278 as in steady flows, and drag reduction in this limit is still only dependent on Ca . On the other hand,
 279 when $L \gg 1$, the blade length is much larger than the wave excursion, so we expect that only
 280 the tip moves with the wave orbital velocity. The majority of the plant is akin to a rigid blade,
 281 and drag reduction is proportional to the product CaL .

282 Unlike seagrasses, kelp rigidity is very low (the stipe is very flexible), while buoyancy is
 283 very high. Therefore, drag forces are primarily balanced by buoyancy. As a result, for most wave
 284 conditions, stiffness plays an insignificant role in kelp motion (i.e, $Ca \gg 1$ and $B \gg 1$). Thus,
 285 for our cases, the buoyancy parameter

$$286 \quad P = \frac{\frac{1}{2}\rho_w C_d A U_w^2}{(\rho_w - \rho_k)gV} = \frac{Ca}{B}, \quad (13)$$

287 first introduced by Nikora et al. (1998) is more relevant. Note that P is equivalent to Ca , except
 288 it measures the magnitude of the drag force in comparison to the resistance to bending provided
 289 by buoyancy. This definition is consistent with Henderson (2019), which built on previous re-
 290 sults to develop a framework for the analysis of the response of aquatic vegetation to wave forc-
 291 ing in the presence of both buoyancy and stiffness. In particular, they identified the joint impor-
 292 tance of CaL and PL in governing plant motion and drag reduction.

293 All of the studies discussed above start from the assumption that the Keulegan-Carpenter
 294 number is large and that the drag force is the main driver of blade motion. As we will show later,
 295 in many of our simulations, inertial forces are larger than the drag forces. To characterize this ef-
 296 fect, we define the Keulegan-Carpenter number as

$$297 \quad KC = \frac{\frac{1}{2}\rho_w C_d U_w^2}{\rho_w d(1 + C_a)U_w \omega} = \frac{C_d}{2(1 + C_a)} \frac{U_w}{\omega d}, \quad (14)$$

298 where d is a thickness associated with the cross sectional area ($d = V/A$). This specific def-
 299 inition, instead of the more traditional $KC = 2\pi U_w / (\omega d)$, is motivated by the scale analysis
 300 of the equations of frond motion and will be further discussed in Sec. 2.3.1.

301 For the wave and kelp conditions studied here, the values of B lie in the range of $O(10^3) <$
 302 $B < O(10^6)$, indicating that buoyancy forces are the dominant restoring forces preventing mo-

Table 2. List of numerical simulations and their associated dimensionless parameters defined in Equations (13), (11), and (14). Wave periods of 5 s, 10 s, 15 s, 20 s correspond with wave numbers of 0.167 m^{-1} , 0.063 m^{-1} , 0.04 m^{-1} , 0.03 m^{-1} , respectively.

H_s [m]	T_p [s]	$l = 2$ [m]			$l = 5$ [m]			$l = 10$ [m]		
		P	L	KC	P	L	KC	P	L	KC
0.25	5	0.0094	57.2	0.071	0.011	130.0	0.078	0.021	189.9	0.11
0.25	10	0.044	13.3	0.31	0.045	32.7	0.31	0.050	62.2	0.33
0.25	15	0.054	8.0	0.51	0.054	19.8	0.51	0.056	38.8	0.52
0.25	20	0.055	5.9	0.69	0.056	14.7	0.69	0.057	29.0	0.70
0.5	5	0.038	28.6	0.14	0.045	65.0	0.16	0.085	95.0	0.21
0.5	10	0.18	6.6	0.61	0.18	16.3	0.62	0.20	31.1	0.65
0.5	15	0.22	4.0	1.02	0.22	9.9	1.03	0.23	19.4	1.05
0.5	20	0.22	2.9	1.38	0.22	7.3	1.40	0.23	14.5	1.40
1	5	0.15	14.3	0.28	0.18	32.5	0.31	0.34	47.5	0.43
1	10	0.70	3.3	1.23	0.72	8.2	1.24	0.79	15.6	1.31
1	15	0.86	2.0	2.04	0.87	5.0	2.05	0.90	9.7	2.09
1	20	0.89	1.5	2.76	0.89	3.7	2.77	0.91	7.2	2.80
2	5	0.60	7.2	0.57	0.73	16.3	0.63	1.36	23.7	0.86
2	10	2.80	1.7	2.45	2.88	4.1	2.49	3.17	7.8	2.61
2	15	3.43	1.0	4.08	3.47	2.5	4.1	3.61	4.9	4.18
2	20	3.55	0.74	5.53	3.57	1.8	5.54	3.65	3.6	5.61

303 tion and that bending stiffness can be safely neglected (see also discussion in the appendix). The
 304 corresponding values of the Cauchy number are $O(10) < Ca < O(10^6)$. Thus, the relevant
 305 parameters characterizing our simulations are P , L , and KC , and values are listed on Table 2.

306 2.3.1 Scaling

307 To gain some insight into frond behavior, we follow the approach used by Henderson (2019)
 308 and start from a horizontal force balance of the governing equation of frond motion, Eq. (7). Here,
 309 we write the equation for the entire kelp frond, as opposed to the discrete version we use in the
 310 numerical model. In particular, Henderson (2019) assumes an equilibrium (i.e., a force balance
 311 with no frond acceleration) and neglects the vertical velocities. Instead, we keep the horizontal

312 acceleration term and write Eq. (7) as

$$\begin{cases}
 (\rho_k + C_a \rho_w) \frac{du_k}{dt} = \frac{1}{2} \rho_w C_d \frac{A}{V} |u_x - u_k| (u_x - u_k) + (\rho_w + C_a \rho_w) \frac{\partial u_x}{\partial t} + \frac{EA_c}{V} \left(\frac{|\mathbf{x}| - l}{l} \right) \sin \theta \\
 -(\rho_k - \rho_w)g + \frac{EA_c}{V} \left(\frac{|\mathbf{x}| - l}{l} \right) \cos \theta = 0
 \end{cases}
 \quad (15)$$

313
 314 Here, θ is the angle of deflection from the vertical, u_x is the representative horizontal wave ve-
 315 locity at the frond tip, u_k is the horizontal component of the tip velocity of the kelp $d\mathbf{x}/dt$, and
 316 \mathbf{x} is the position of the frond tip. We proceed by assuming that θ is small enough so that the small
 317 angle approximation $\cos \theta \approx 1$ can be invoked, reducing the vertical balance in (15) to

$$(\rho_k - \rho_w)g = \frac{EA_c}{V} \left(\frac{|\mathbf{x}| - l}{l} \right) \quad (16)$$

319 which yields the new horizontal balance

$$(\rho_k + C_a \rho_w) \frac{du_k}{dt} = \frac{1}{2} \rho_w C_d |u_x - u_k| (u_x - u_k) + (\rho_w + C_a \rho_w) \frac{\partial u_x}{\partial t} + (\rho_k - \rho_w)g \frac{x}{l} \quad (17)$$

321 Note that we also used $\sin \theta = x/l$.

322 Normalizing by ρ_w , U_w , ω , and Δx_w , Eq. (17) can be written as

$$\frac{PL}{KC} \left[\frac{du_k^*}{dt^*} - \frac{\partial u_x^*}{\partial t^*} \right] = PL \left[|u_x^* - u_k^*| (u_x^* - u_k^*) \right] + [x^*], \quad (18)$$

324 where we used the approximation $\frac{(\rho_k/\rho_w + C_a)}{(1+C_a)} \approx 1$. Here, all the terms denoted by $*$ are dimen-
 325 sionless and assumed to be of order unity.

326 The equivalent equation for the force balance (i.e., assuming no acceleration) as done in
 327 Henderson (2019) is given by

$$\frac{PL}{KC} \left[-\frac{\partial u_x^*}{\partial t^*} \right] = PL \left[|u_x^* - u_k^*| (u_x^* - u_k^*) \right] + [x^*]. \quad (19)$$

329 The more complete Eq. (18) and its force balance version (19) both suggest the use of PL
 330 and PL/KC as two main scaling parameters. A visualization of this two-dimensional parame-
 331 ter space is given in Fig. 3.

332 It is useful to understand the behavior of kelp fronds in three asymptotic regimes: (1) the
 333 “buoyancy dominated” regime, given by $PL \ll 1$ and $PL/KC \ll 1$ and corresponding to points
 334 in the red region and closer to the origin in Fig. 3(a), (2) the “drag dominated” regime, given by
 335 $PL \gg 1$ and $KC \gg 1$ and corresponding to points in the blue region and closer to the bottom
 336 right corner of Fig. 3(a), and (3) the “inertia dominated” regime, given by $PL/KC \gg 1$ and
 337 $KC \ll 1$ and corresponding to points in the yellow region and closer to the top left corner of
 338 Fig. 3(a).

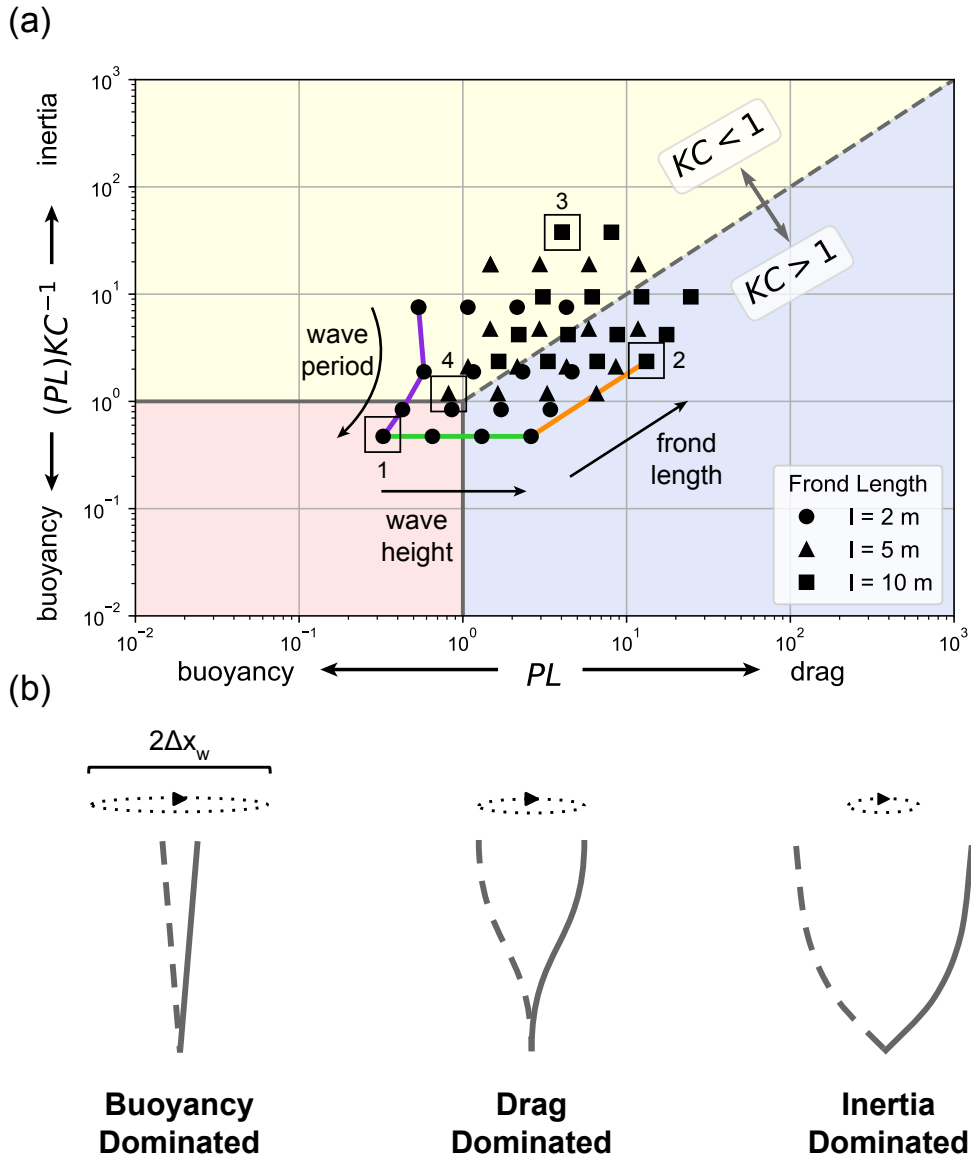


Figure 3. (a) The parameter space for kelp motion. The red region represents where motion is buoyancy dominated; blue represents where motion is drag dominated; yellow represents where motion is inertia dominated. The gray lines represent the dividers $PL = 1$, $PL/KC = 1$, and the dashed gray line is $KC = 1$. The black points are where our simulations fall, where different shapes represent each of the plant lengths. The purple, green, and orange solid lines show increasing wave period, wave height, and plant length, respectively. Black squares 1, 2, 3, and 4 denote cases selected for further analysis in later sections. (b) Expected kelp motion in each asymptotic regime.

339 In the “buoyancy dominated” regime, Eq. (18) suggests $x^* \ll 1$, which implies $x \ll \Delta x_w$
 340 (i.e., Δx_w is not the appropriate scale for the horizontal excursion of the tip). Here, buoyancy is
 341 very strong and severely limits plant motion as depicted in Fig. 3(b). This is equivalent to the nearly
 342 rigid plant configuration considered by both Luhar and Nepf (2016) and Henderson (2019).

343 The “drag dominated” regime corresponds to the small excursion limit of Luhar and Nepf
 344 (2016) and Henderson (2019). Here, drag forces are much larger than inertial forces and the frond
 345 motion is driven mostly by drag. In this case, the left hand side of Eq. (18) is approximately 0,
 346 resulting in the following simplification:

$$347 \quad |u_x^* - u_k^*|(u_x^* - u_k^*) = \frac{|x^*|}{PL}. \quad (20)$$

348 Since $PL \gg 1$, it is expected that cases in this regime should have small relative velocity, or
 349 that $|u_x^* - u_k^*|(u_x^* - u_k^*) \ll 1$. The frond should move closely with the wave motion, meaning
 350 that $x^* \approx 1$, or $x \approx \Delta x_w$ as illustrated in Fig. 3(b).

351 Finally, in the “inertia limit”, inertial forces are much larger than drag and buoyancy. Thus,
 352 we can assume that

$$353 \quad \frac{PL}{KC} \left[\frac{du_k^*}{dt^*} - \frac{\partial u^*}{\partial t^*} \right] \gg PL [|u_x^* - u_k^*|(u_x^* - u_k^*)], \quad (21)$$

354 and applying that simplification to Eq. (18) yields

$$355 \quad \frac{PL}{KC} \left[\frac{du_k^*}{dt^*} - \frac{\partial u^*}{\partial t^*} \right] = [x^*]. \quad (22)$$

356 Because $PL/KC \gg 1$, this requires

$$357 \quad \left[\frac{du_k^*}{dt^*} - \frac{\partial u^*}{\partial t^*} \right] \propto \left(\frac{PL}{KC} \right)^{-1}, \quad (23)$$

358 implying that the two accelerations are of the same order of magnitude. In practice, this means
 359 that the frond acceleration is mostly caused by the same pressure gradient force that is driving
 360 the wave motion. Because kelp is less dense than the fluid ($\rho_k < \rho_w$), the frond acceleration
 361 in response to the same pressure gradient force is larger than that of a fluid parcel, causing the
 362 frond to perform an orbital motion with larger horizontal displacements than the fluid itself. Hence,
 363 when $PL/KC \gg 1$, we also have $x^* = x/\Delta x_w > 1$, meaning that it is possible for the kelp ex-
 364 cursion to be greater than the wave excursion.

365 **2.3.2 Drag Coefficient Scaling**

366 The varying flexibility of aquatic vegetation can reduce the drag force exerted on the flow
 367 by two mechanisms: (1) a reduction of the frontal area exposed to the flow, and (2) a reduction

368 in the relative velocity due to synchronous motion of vegetation and water. Luhar and Nepf (2011)
 369 quantified this effect by defining the effective length, l_e , which represents the length of a rigid
 370 blade that generates the same drag as a flexible blade of length l . Physically, l_e/l represents the
 371 ratio of the real horizontal drag force (F_D) to the horizontal drag force experienced by a rigid blade
 372 ($F_{D,Rig}$). Alternatively, it is equivalent and sometimes more convenient to define a reduced drag
 373 coefficient $C_{d,f}$ to represent the effect of motion on the drag force (Razmi et al., 2020), or

$$374 \quad \frac{l_e}{l} = \frac{F_D}{F_{D,Rig}} = \frac{C_{d,f}}{C_d}. \quad (24)$$

375 If $C_{d,f}$ is known, one can calculate the true drag force using the fluid velocity (without explicit
 376 knowledge of the vegetation motion) via

$$377 \quad F_D = \frac{1}{2} \rho_w C_{d,f} A |u_x| u_x. \quad (25)$$

378 The drag reduction due to plant motion is modeled by the reduced value of $C_{d,f}$ (when compared
 379 to C_d).

380 Luhar and Nepf (2016) found that for plants where the restoring force is primarily from the
 381 bending rigidity, $C_{d,f}/C_d \propto (CaL)^{-1}$. Henderson (2019) considered the case with both bend-
 382 ing rigidity and buoyancy when the motion is driven by a linearized drag force. Their solution
 383 recovers the result from Luhar and Nepf (2016) when buoyancy is negligible and yields a new
 384 result for the case of interest here, where buoyancy is the dominant restoring mechanism. In this
 385 case, their result yields

$$386 \quad \frac{C_{d,f}}{C_d} = \left[\frac{\pi^2/(4PL)^2}{1 + \pi^2/(4PL)^2} \right]^{1/4}, \quad (26)$$

387 which transitions from a region in which $C_{d,f}/C_d \approx 1$ in the buoyancy dominated regime to
 388 $C_{d,f}/C_d \propto (PL)^{-1/2}$ for large PL in the drag dominated regime. Previous studies did not con-
 389 sider the cases where inertia is important ($KC \ll 1$), and it is unclear how that would impact
 390 the total drag force.

391 **2.3.3 Parameter Space**

392 The cases shown in Table 2 are presented on the parameter space formed by PL and PL/KC
 393 in Fig. 3. For most wave conditions, our simulations are in a transition region ($KC \approx 1$, $PL \approx$
 394 1 , or $PL/KC \approx 1$), so we do not expect to observe results that resemble the asymptotic con-
 395 ditions discussed in Section 2.3.1. Note that most studies to date have focused on the regime in
 396 which $KC \gg 1$, investigating motion and drag in the transition between the red and blue regions.

397 To facilitate interpretation of our results presented in the next sections, we have included
 398 in Fig. 3 arrows indicating how varying wave properties and frond length impact the location of
 399 points on the parameter space. Wave orbital velocity amplitudes are proportionate to $A_w\omega$, so
 400 larger wave periods (and smaller wavenumbers) generally leads to smaller PL and larger KC val-
 401 ues. In other words, increasing wave period (reducing wavelength) results in cases where buoy-
 402 ancy is relatively larger and drag is more important than inertial forces. Lines of increasing wave
 403 height have constant PL/KC values (parallel to the x -axis in Fig. 3), transitioning further away
 404 from the limiting behavior of buoyancy or inertia dominated regimes into the drag dominated regime.
 405 Similarly, only increasing frond length does not affect KC , but correlates with increasing PL and
 406 PL/KC values, meaning buoyancy becomes relatively less important.

407 3 Results and Discussion

408 3.1 Characterization of Kelp Motion

409 In general, model kelp responded to different wave conditions with a wide range of behav-
 410 ior. Initially, all upright fronds undergo an adjustment period that lasts a few wave periods be-
 411 fore they reach an equilibrium cycle, the type of which depends on where the simulation falls in
 412 the parameter space of Fig. 3(a).

413 Fig. 4 shows example frond excursion plots for different regimes of kelp motion: buoyancy
 414 dominated, drag dominated, inertia dominated, and a transition case (refer back to Figure 3(a)
 415 for where each case is located in the parameter space). Animations for these four cases are pre-
 416 sented in the Supporting Information. For each case, we also show how the relative horizontal
 417 frond excursion

$$418 \delta x = \frac{(x_{\max} - x_{\min})}{2\delta x_w(\bar{z})} \quad (27)$$

419 varies along the length of the plant. Here, $2\delta x_w(\bar{z})$ is the local horizontal wave excursion at the
 420 mean vertical position of each segment over the wave cycle, or

$$421 \delta x_w(\bar{z}) = A_w\omega \cosh(k\bar{z})/\sinh(kH) \quad (28)$$

422 Physically, δx is a measure of the frond excursion normalized by the average wave excursion.

423 In the buoyancy dominated region of the parameter space (Case 1, Fig. 4a), the frond ex-
 424 cursion is less than the wave excursion as the entire frond remains mostly upright. The maximum
 425 frond excursion is <90% of the horizontal wave excursion. In this case, $PL \approx 0.3$ and $(PL)/KC \approx$
 426 0.5, so buoyancy is only around 2-3 times larger than the other forces, which is why the blade ex-

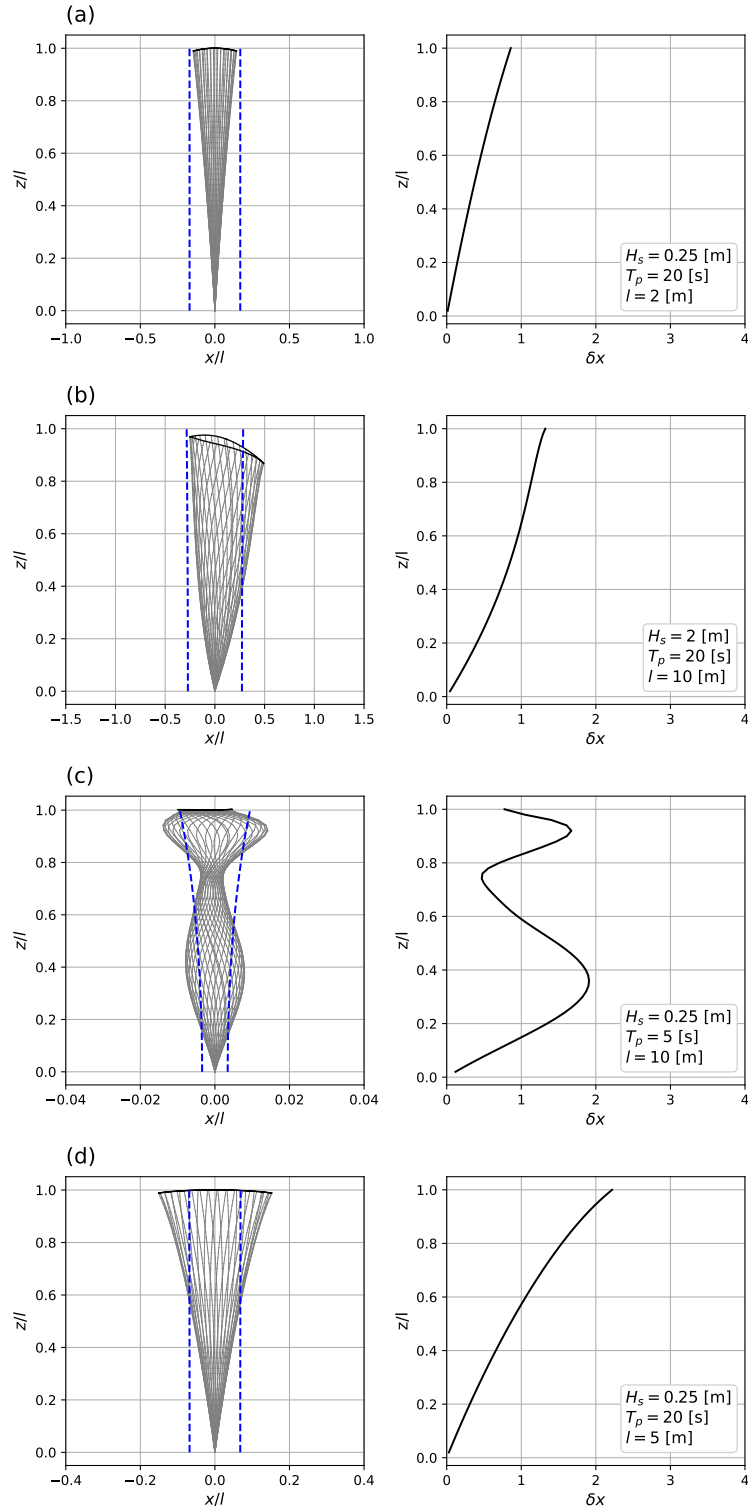


Figure 4. The cases of kelp motion from different regions of the parameter space; see Figure 3(a). Left panels are blade excursions over one equilibrium wave cycle; blue dashed lines represent the horizontal wave excursion at each depth. Both axes are normalized by plant length (l). Right panels are relative horizontal excursion plots for the buoyancy dominated case. (a) Case 1: buoyancy dominated. (b) Case 2: drag dominated. (c) Case 3: inertia dominated. (d) Case 4: transition.

427 excursion is still fairly large. As points move farther into the buoyancy dominated regime (closer
 428 to the origin in the parameter space), we expect that the maximum blade excursion would decrease
 429 to nearly zero.

430 For drag dominated cases (Case 2, Fig. 4b), the upper half of the frond moves more-or-less
 431 with the wave, while the bottom portion of the frond moves less than the wave excursion around
 432 it. A slight concavity in the profile of δx indicates that the majority of drag is being generated
 433 in the bottom 50% of the frond, as postulated by Henderson (2019). There is a part of the tip that
 434 moves about 30% more than the wave, which we hypothesize may be the additional effects of the
 435 inertial forces or asymmetric motion. Overall, this is the classic example of drag reduction in flex-
 436 ible vegetation due to synchronous oscillation with the wave motion (i.e., reduction in relative
 437 velocity between the frond and the water).

438 In the inertia dominated limit (Case 3, Fig. 4c), a majority of the frond (around 60%) moves
 439 more than the wave excursion. Note that the displacements are only a small fraction of the plant
 440 length, and that the aspect ratio of the figure is highly distorted. The maximum frond excursion
 441 is almost twice as large as the wave excursion; this is clearly a much greater effect than in the pre-
 442 vious two cases. Different portions of the frond are out of phase with each other (the animation
 443 included in Supporting Information is particularly illuminating here), corresponding to a higher
 444 natural mode of vibration. This would be equivalent to mode 2 motion identified by Mullarney
 445 and Henderson (2010). This higher mode leads to a non-monotonic variation of the amplitude
 446 of the frond motion along its length, and we hypothesize that higher inertial forces potentially
 447 lead to the amplification of higher natural modes of motion.

448 Finally, we included a typical example of our transition cases (Case 4, Fig. 4d). Here, the
 449 frond excursion plots displays a mix of traits from the other three limits. About half of the frond
 450 moves more than the wave, with the tip moving over twice as much as the fluid does. The frond
 451 also stays relatively upright and straight, as in the buoyancy dominated regime. Unlike the in-
 452 ertia dominated example, there is a smooth transition in the amplitude of kelp motion.

453 Despite the large variation in frond motion depending on the dominant forcing mechanisms,
 454 some general conclusions are possible. For a fixed frond length l , the relative horizontal blade
 455 excursion δx decreases with increasing KC . When $KC < 1$ (inertial forces are larger than drag
 456 forces), the entire frond moves more than the wave excursion. On the other hand, when $KC >$
 457 1, a majority of the frond moves less than the wave, with the tip moving about the same. Figure
 458 5 illustrates how the average of δx over the frond length, denoted $\overline{\delta x}$, varies with KC . Clearly,

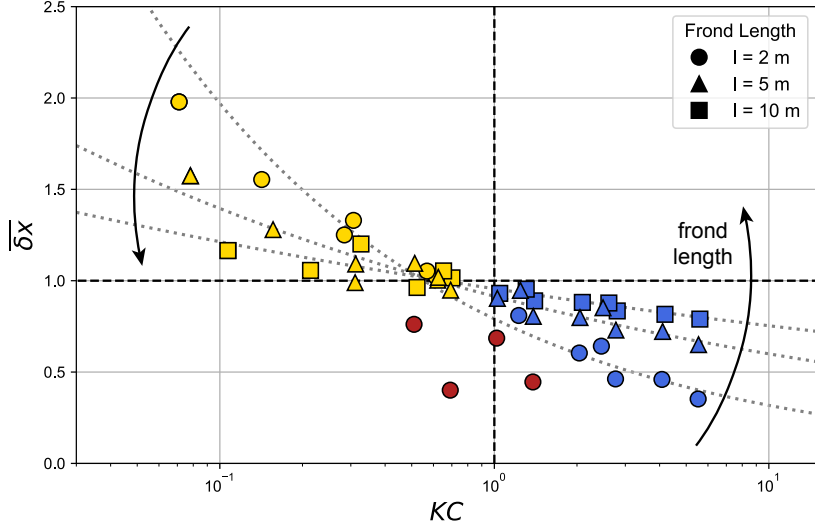


Figure 5. Variation in relative horizontal excursion, averaged over length of the blade ($\overline{\delta x}$) with KC . Yellow points are inertia dominated ($PL/KC > 1$ and $KC < 1$), red are buoyancy dominated ($PL < 1$ and $PL/KC < 1$), and blue are drag dominated ($PL > 1$ and $KC > 1$). Different shapes represent different frond lengths, with circles representing 2 m fronds, triangles are 5 m, and squares are 10 m. Dashed lines were added to facilitate interpretation.

459 for each frond length, $\overline{\delta x}$ reduces with increasing KC . The buoyancy dominated cases (red sym-
 460 bols) appear as outliers, having much smaller excursions than suggested by the behavior of neigh-
 461 boring points.

462 Luhar and Nepf (2016) described the relative blade excursion for seagrasses (bending resis-
 463 tance being the dominant restoring force) in the large KC (drag dominated) regime. In par-
 464 ticular, they argued that $\overline{\delta x} \approx 1$ for $L \gg 1$ and $\overline{\delta x} \ll 1$ for $L \ll 1$. Note that in our cases,
 465 Eqs. (11) and (14) imply $L \propto (l/d)KC^{-1}$. Since we keep the stipe diameter d constant in all
 466 our simulations, at a constant value of KC we have $L \propto l$. Results in Fig. 5 agree with Luhar
 467 and Nepf (2016) for the large KC regime ($KC > 1$, represented by blue symbols), in that at a
 468 fixed value of KC , $\overline{\delta x}$ increases with increasing L and approaches $\overline{\delta x} \approx 1$ for large L . Inter-
 469 estingly, all the frond lengths seem to match the wave excursion for $KC \approx 0.7$, and the behavior
 470 switches for values of KC below this threshold (i.e., in the inertia dominated regime) where fronds
 471 have larger excursions than the water and $\overline{\delta x}$ increases with decreasing L . In this small KC regime,
 472 $\overline{\delta x} \approx 1$ still holds for large L , but $\overline{\delta x} \gg 1$ for $L \ll 1$. Therefore, the unifying conclusion from
 473 Fig. 5 valid across the entire KC regime is that $\overline{\delta x} \approx 1$ for $L \gg 1$, and deviations increase with

474 increasing L in different directions depending on the dominant forcing mechanism (drag vs. in-
 475 ertia).

476 3.2 Characterization of Drag Forces

477 In our numerical simulations, the drag force is a function of position along the frond and
 478 time. We follow Luhar and Nepf (2016) and integrate the horizontal drag force over the frond
 479 length, and take its root mean square (RMS) value over one wave cycle to characterize the total
 480 drag for each simulation. We verified that as tested by Luhar and Nepf (2016), using the max-
 481 imum value over the cycle here as well does not produce significant changes. Therefore, we cal-
 482 culate the drag reduction as

$$483 \frac{C_{d,f}}{C_d} = \frac{[F_D]_{RMS}}{[F_{D,Rig}]_{RMS}} = \frac{\left[\int_0^l \frac{1}{2} \rho_w C_d a |\mathbf{u} - \frac{d\mathbf{x}}{dt}| (u_x - \frac{dx}{dt}) dl \right]_{RMS}}{\left[\int_0^l \frac{1}{2} \rho_w C_d a |\mathbf{u}| u_x dz \right]_{RMS}}, \quad (29)$$

484 where $a = A/l$ is the maximal frond projected area per unit length (i.e., the frond area density).

485 Resulting values of $C_{d,f}/C_d$ are displayed as a function of PL and separated by drag dom-
 486 inated ($KC \leq 1$) and inertia dominated ($KC > 1$) regimes in Fig. 6a. As expected, there is
 487 good agreement between our drag-dominated cases ($KC > 1$, circles) and the prediction from
 488 Henderson (2019) given by Eq. 26. Our own power-law fit to these cases yields

$$489 C_{d,f}/C_d = (PL)^{-0.6} \quad (30)$$

490 across the entire range of PL , extending to values larger than 1 for $PL < 1$ (to be discussed be-
 491 low). The small difference in exponent likely originates, among other things, from the linearized
 492 drag approximation employed in the derivation of (26) and the presence of inertial forces in our
 493 simulations.

494 On the other hand, the inertia dominated cases ($KC < 1$, triangles) do not scale as well
 495 with Eq. (26). Generally, values of $C_{d,f}/C_d$ seem to be independent of KC in the range $PL <$
 496 1, but the power-law decay in the large PL region is steeper for the inertia dominated cases. We
 497 expect the drag reduction to be a joint function of PL and KC , but unfortunately our simulated
 498 cases are not enough to support a two-dimensional fit with any confidence. Instead, we note that
 499 both Eq. (26) and the empirical fit (30) can serve as an upper bound on the true drag. Our best
 500 fit for the inertia dominated cases yields $C_{d,f}/C_d = 0.7(PL)^{-0.8}$.

501 Two important features of Fig. 6 require further explanation: the larger drag reduction in
 502 the inertia dominated cases and the increase in drag compared to a rigid frond (i.e. drag augmen-

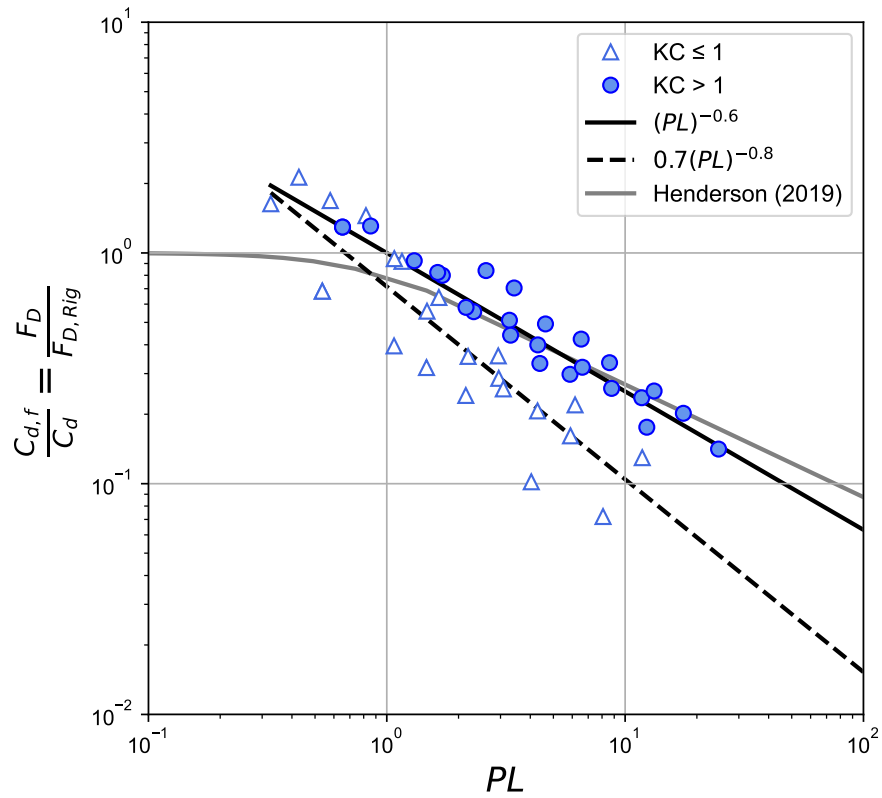


Figure 6. Effective drag coefficients calculated using horizontal drag force only versus PL . The solid black line is the best fit ($R^2 = 0.92$) for cases where $KC > 1$, while the dashed black line is the best fit ($R^2 = 0.86$) for $KC < 1$. The gray line represents Eq. (26). Triangles represent cases where $KC < 1$, while circles are cases where $KC > 1$.

503 tation) for most cases in which $PL < 1$. To address these questions, we note once again that in
 504 our model all changes to drag are caused by the relative velocity between the frond and the wa-
 505 ter. We define a normalized relative velocity

$$506 \quad u_{rel} = \frac{(u_x - dx/dt)}{U_w}, \quad (31)$$

507 and show the variation of u_{rel} over one equilibrium wave period at several locations along the
 508 frond in Fig. 7 for the four sample cases illustrated in Fig. 4 (refer to Fig. 8b for the specific $C_{d,f}/C_d$
 509 value corresponding to the cases shown in Fig. 7).

510 In a typical drag dominated case, the upper portion of the frond moves with the waves, re-
 511 ducing the relative velocities towards the frond tip (e.g., see Figure S1 of the Supporting Infor-
 512 mation). In this case, most of the drag originates from the bottom of the frond where the rela-
 513 tive velocities are comparable to the wave velocity due to restricted frond motion (Luhar & Nepf,
 514 2016; Henderson, 2019). In our selected drag dominated case (Fig. 7b), the behavior is already
 515 more complex than that. The relative velocity at a given time switches sign between the bottom
 516 and the top of the frond (e.g., at $t/T_p = 0.5$ we have $u_{rel} > 0$ at $z/l = 0.2$ and $u_{rel} < 0$ at
 517 $z/l = 1.0$). This change in sign occurs when the frond velocity in the upper portion of the frond
 518 is larger than the wave velocity, which happens when the frond excursion is larger than that of
 519 the fluid as described in the previous subsection (see Fig. 4b). The cancellation between drag forces
 520 from the top and bottom of the frond lead to additional drag reduction in comparison to the typ-
 521 ical case described above, and it may also in part explain the steeper $(PL)^{-0.6}$ decay of $C_{d,f}/C_d$
 522 in comparison to the prediction by Henderson (2019).

523 In order to explain the drag augmentation that occurs for most cases with $PL < 1$, we con-
 524 trast the classic drag reduction behavior to that observed for the buoyancy dominated case in Fig.
 525 7a (which has $C_{d,f}/C_d \approx 1.6$, as seen in Fig. 8b). Here we notice that, contrary to expectations,
 526 the relative velocity (and therefore the drag force) monotonically increases from the bottom to
 527 the top of the frond. This is only possible if the frond velocity is out-of-phase with the water ve-
 528 locity so that $(u_x - dx/dt) > u_x$ (e.g., when $u_x > 0$, we must have $dx/dt < 0$ for this to be
 529 possible). In this case, most of the drag actually comes from the tip of the frond, and the total drag
 530 is larger than that of a rigid frond, yielding $C_{d,f}/C_d > 1$. Therefore, we conclude that drag aug-
 531 mentation is a physical feature of flexible vegetation that occurs when the frond motion is out-
 532 of-phase with the wave orbital velocity and it must also be taken into account. This out-of-phase
 533 motion is caused by inertial forces (note that the pressure gradient force is 90 degrees out of phase
 534 with the wave motion).

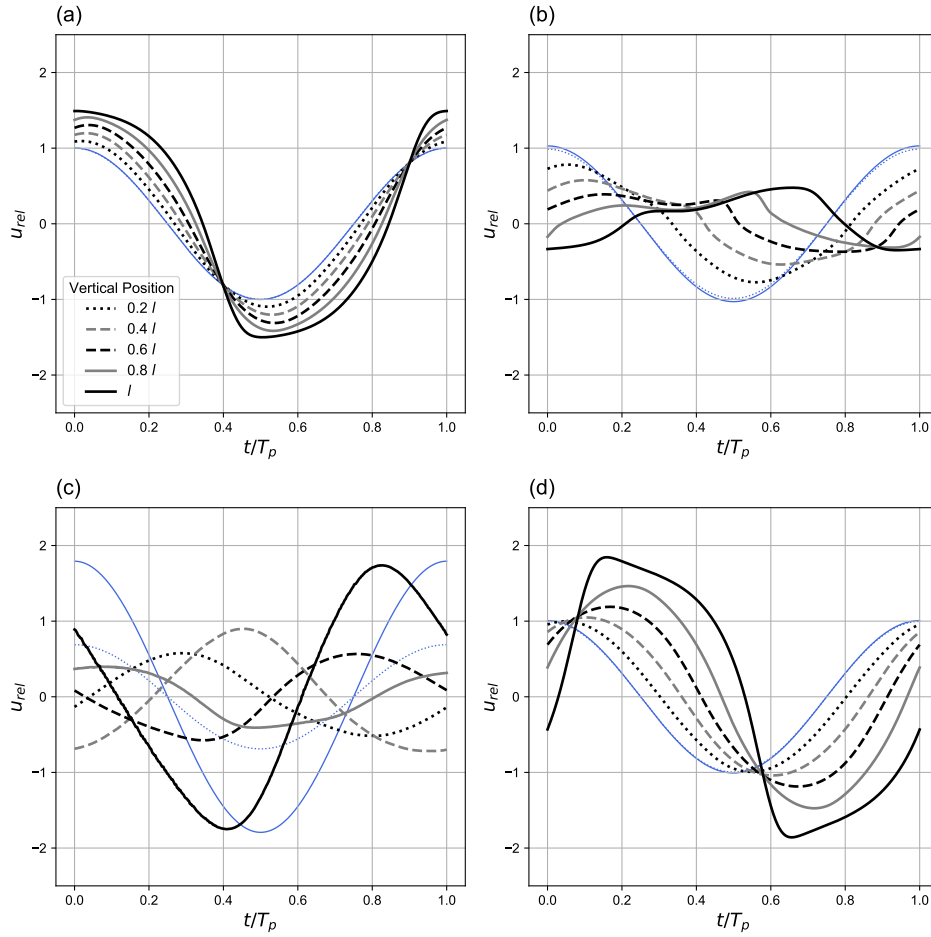


Figure 7. Relative velocities at five different locations along the length of the blade ($0.2l$, $0.4l$, $0.6l$, $0.8l$, and l) over the course of one wave cycle for each case of frond motion. Solid and dotted blue lines indicate the fluid velocity at the tip of the frond and at $0.2l$, respectively. All velocities are normalized by U_w . (a) Case 1: buoyancy dominated, $H_s = 0.25$ [m], $T_p = 20$ [s], $l = 5$ [m]. (b) Case 2: drag dominated, $H_s = 2$ [m], $T_p = 20$ [s], $l = 10$ [m]. (c) Case 3: inertia dominated, $H_s = 0.25$ [m], $T_p = 5$ [s], $l = 10$ [m]. (d) Case 4: transition, $H_s = 0.25$ [m], $T_p = 20$ [s], $l = 5$ [m].

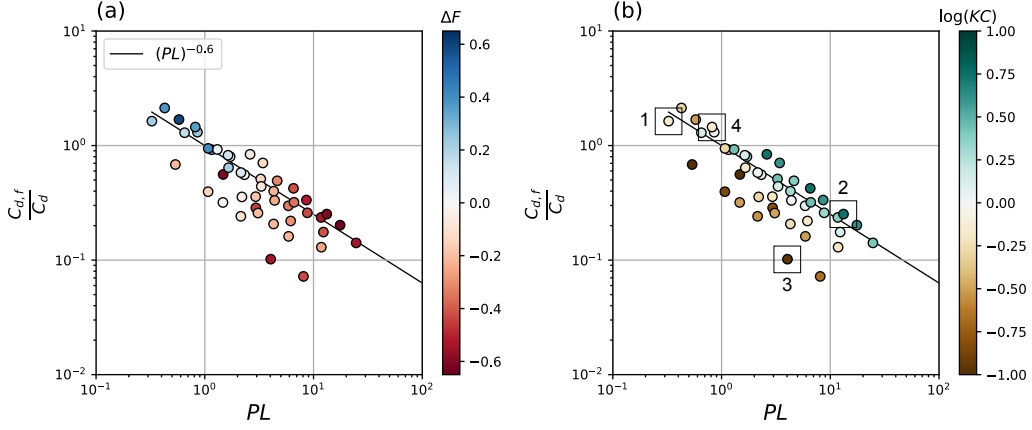


Figure 8. (a) $C_{d,f}/C_d$ versus PL , where points are colored by $\log(KC)$. Positive color values indicate $KC > 1$, while negative values represent points with $KC < 1$. (b) $C_{d,f}/C_d$ versus PL , where points are colored by $\Delta F_{D,l}$, which quantifies the difference between the drag exerted by the bottom half of the plant and the top half. Black squares 1, 2, 3, and 4 represent the same cases referenced in 3a. In both panels, the black line is the same best fit as in Fig. 6.

535 To further characterize this behavior, we define the parameter

$$536 \quad \Delta F = \frac{[F_{D,top}]_{RMS} - [F_{D,bot}]_{RMS}}{[F_{D,top}]_{RMS} + [F_{D,bot}]_{RMS}} \quad (32)$$

537 where $[F_{D,top}]_{RMS}$ and $[F_{D,bot}]_{RMS}$ are the RMS of the drag integrated over the top half and
 538 bottom half of the frond. When ΔF is positive, more drag is generated by the top half of the frond
 539 than the bottom half; the opposite is true when ΔF is negative. Figure 8a shows $C_{d,f}/C_d$ against
 540 PL , but with points colored by ΔF . All the points with $C_{d,f}/C_d > 1$ have positive ΔF values,
 541 meaning that a majority of the drag is originated from the top half of the frond, thus implying out-
 542 of-phase motion between frond and water. In our most extreme case, the drag force from the up-
 543 per half of the frond is almost four times as large as that of the bottom half. We have verified that
 544 all these cases with drag augmentation have relative velocity profiles similar to the one shown
 545 in Fig. 7a.

546 As previously discussed, the drag force decays even faster than $(PL)^{-0.6}$ in the inertia dom-
 547 inated cases. For the case illustrated in Fig. 7c, we see that the drag force changes sign twice be-
 548 tween the bottom and the top of the frond. This is in part associated with the complex behavior
 549 associated with the higher natural mode that corresponds to the motion of these cases (see Fig.
 550 4c). The large cancellations of the drag force along the frond in these cases with $KC < 1$ lead
 551 to much smaller values of the total drag in comparison to other cases. This is clearly seen in Fig.

8b, where $C_{d,f}/C_d$ is displayed against PL and colors represent their value of $\log KC$. Positive color values represent simulations where $KC > 1$, and negative color values represents simulations where $KC < 1$. There is generally a smooth decrease in KC as points move farther away from the best fit line for the large KC regime, suggesting a smooth reduction in $C_{d,f}/C_d$ with decreasing KC . As a result, this type of motion appears even more “flexible” than in the drag dominated regime. Note also that these inertia dominated cases tend to have more drag originating from the bottom of the frond or, at most, an even distribution between top and bottom drag (see Fig. 8a).

Finally, our transition case (Fig. 7d) displays a mix of traits from the three aforementioned cases, including increased drag from the upper portion of the frond due to out-of-phase motion with the water (and associated $C_{d,f}/C_d > 1$) and a switch in sign of the drag along the frond due to larger frond excursions in comparison to water parcels. For more elaboration on how to interpret Fig. 7, please refer to Figure S1 of the Supporting Information.

3.3 Asymmetric Motion

Another interesting aspect of flexible vegetation motion is the degree of asymmetry, even under symmetric wave forcing. Zhu et al. (2020) conducted an in depth analysis of the conditions for asymmetric blade motion, concluding that there are only a few conditions where blade motion is nearly symmetric: (1) when blade length is much smaller than the wavelength $\lambda = 2\pi/k$, (2) blade length is much smaller than the water depth, or (3) the water depth is much smaller than the wavelength. In our simulations, wavelengths vary between $\lambda = 37$ m and $\lambda = 210$ m, so the vast majority of our cases satisfy both (1) and (3) and we would expect symmetric frond motion. Zhu et al. (2020) quantified degree of asymmetry defining $\beta_{xT} = \bar{x}/|x_{\max}|$, where \bar{x} is the average displacement over an equilibrium cycle and $|x_{\max}|$ is the maximum horizontal displacement (they also used an arbitrary threshold $\beta_{xT} < 0.05$ for nearly symmetric motion). Based on the values of $|\beta_{xT}|$ shown in Fig. 9, most of our simulations display asymmetric motion. A few of our cases with $KC \leq 1$ had negative β_{xT} values, meaning that \bar{x} is slightly negative even though the wave propagates in the positive x direction. This is likely due to the effects of inertial forces being out of phase with drag. To include these points, we chose to plot the absolute value of β_{xT} .

Zhu et al. (2020) attributes the cause of asymmetric motion to be either the effect of vertical wave orbital velocities or spatial asymmetry of the encountered wave orbital velocities from

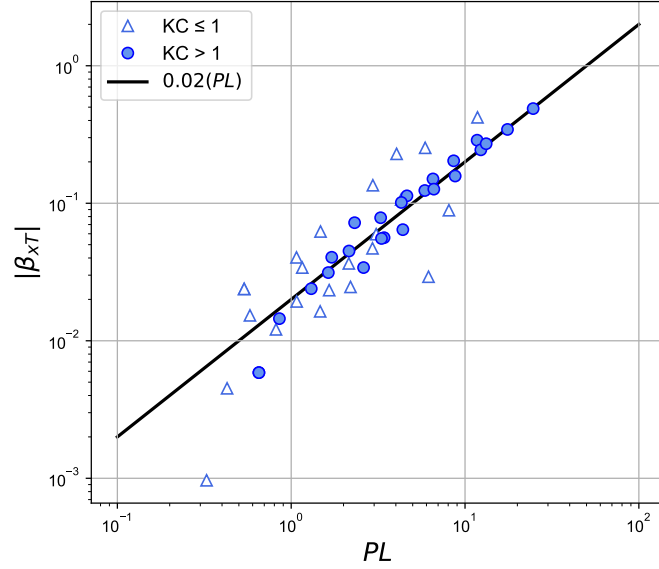


Figure 9. Degree of asymmetry, β_{xT} increases with PL . Blue filled circles are drag dominated cases ($KC > 1$); open triangles are inertia dominated ($KC \leq 1$). Black line represents the best fit for the $KC > 1$ points ($R^2 = 0.94$).

583 horizontal blade displacements. We performed numerical simulations removing these two effects
 584 (i.e., by setting the vertical wave velocity to zero and eliminating the forcing dependence on the
 585 x -position of the nodes) and observed only a very small reduction in the degree of asymmetry
 586 (not shown), suggesting that other mechanisms may be involved in our cases. Nevertheless, it is
 587 remarkable that the parameter PL is an excellent predictor of the degree of asymmetry measured
 588 by β_{xT} . The coefficient of determination (R^2) is larger than that for the drag coefficient reduc-
 589 tion in Fig. 6, and even though the spread is larger for the inertia dominated cases, there seems
 590 to be no trend with KC as in the case of the drag coefficient. Note that increasing PL is mostly
 591 accomplished by increasing wave height, increasing frond length, or reducing buoyancy, condi-
 592 tions that are expected to lead to more asymmetric motion (Zhu et al., 2020). Importantly, the
 593 scaling of $C_{d,f}/C_d$ and β_{xT} with PL suggests that there is a correlation between drag reduction
 594 and motion asymmetry.

595 **4 Conclusion**

596 In this study, we developed a numerical model to investigate the motion of kelp fronds and
 597 its impact on drag forces in response to realistic monochromatic wave forcing. From the wave

598 parameters retrieved from observations, it becomes clear that the usual assumption of weak in-
 599 inertial forces (i.e., large Keulegan-Carpenter number KC) is not always applicable to kelp motion
 600 in nearshore waters. A more detailed scaling analysis of the equations of frond motion suggests
 601 a 2-dimensional parameter space formed by a combination of KC , the buoyancy parameter P ,
 602 and the ratio of frond length to wave horizontal excursion L . Motivated by the governing equa-
 603 tion of motion, we chose to use PL and PL/KC as the two independent parameters. This leads
 604 to 3 asymptotic regimes (dominated by buoyancy, drag, and inertia) and successful classification
 605 of different types of frond motion (see Fig. 3).

606 We quantified the relative horizontal excursion of the frond in comparison to that of wa-
 607 ter, and the results shows strong dependence on KC and L . For the drag-dominated cases (large
 608 KC), frond excursion is smaller than water excursion, and differences increase with increasing
 609 KC and decreasing frond length. This is consistent with the analysis of Luhar and Nepf (2016).
 610 For the inertia dominated cases (small KC), frond excursion is larger than water excursion and
 611 differences increase with decreasing KC and frond length. Interesting, for all frond lengths, frond
 612 excursions match water excursion for $KC \approx 0.7$.

613 We have also investigated the extent that kelp motion impacts its drag reduction (in com-
 614 parison to a rigid kelp frond). We quantify drag reduction by introducing a ratio of the true drag
 615 coefficient to that of a rigid frond $C_{d,f}/C_d$, and found that drag reduction is a function of KC
 616 and PL . Our empirical fit to simulation results yields

$$617 \quad C_{d,f}/C_d = \begin{cases} (PL)^{-0.6} & \text{if } KC > 1 \\ 0.7(PL)^{-0.8} & \text{if } KC \leq 1 \end{cases} \quad (33)$$

618 The result for the drag dominated regime ($KC > 1$) is fairly close to the prediction by Henderson
 619 (2019). The steeper drag reduction with PL in the inertia dominated case ($KC \leq 1$) results from
 620 a reversal of the drag direction along the frond and cancellation between drag forces acting in op-
 621 posite directions. We also observe drag augmentation (i.e., $C_{d,f}/C_d > 1$) for cases in which
 622 $PL < 1$, and track the origin of this to the motion of the frond being out-of-phase with the mo-
 623 tion of the water.

624 It is important to note that drag reduction is directly associated with the efficiency of wave
 625 energy dissipation by the vegetation. As a general conclusion, in the regimes of frond motion stud-
 626 ied here, the effective drag coefficient is reduced with increasing PL and decreasing KC . Waves
 627 with smaller periods correspond to smaller KC and larger PL , and thus smaller drag coefficient

628 and less efficient energy dissipation. Similarly, increasing wave height increases PL (without af-
629 fecting KC), leading to smaller drag.

630 Future research needs to extend the modeling to include effects of mean currents and broad-
631 band wave spectra (and possibly turbulence) on the frond motion, and the presence of surface canopies.
632 In addition, observational confirmation by synchronous measurements of wave and kelp motions
633 are necessary to validate our modeling results.

634 **Appendix A Model Validation**

635 Due to lack of detailed observations of blade/frond motion and drag reduction for cases with
636 negligible bending stiffness that could be used to validate our model assumptions, we test our model
637 against the theory developed by Luhar and Nepf (2011) for bending of flexible blades in steady
638 unidirectional flow. More specifically, we compare model results to the predictions of effective
639 length given by their Equation 16, which includes both bending stiffness and buoyancy as restor-
640 ing forces and can be written in terms of P as

$$641 \quad \frac{l_e}{l} = 1 - \frac{1 - 0.9Ca^{-1/3}}{1 + 8Ca^{-3/2} + P^{-3/2}}. \quad (\text{A1})$$

642 Note that this theory-based expression has empirical constants. We made small adjustments to
643 our numerical model to better match the conditions used in Luhar and Nepf (2011). We mod-
644 ified the drag force to include the frontal area reduction due to blade bending (i.e., including the
645 $\cos \theta$ term), and removed the drag force in the z direction (the relative velocity being defined only
646 based on the x component).

647 Our goal is to test the hypothesis that, for our range of values of Ca and P , neglecting the
648 bending stiffness (i.e., assuming $Ca \rightarrow \infty$) has a negligible effect on the results. Our study de-
649 sign uses all the kelp geometric and constitutive properties described in Section 2.2, neglecting
650 the bending stiffness and still allowing for stretching of the blade. We tested model performance
651 across a wide range of P by varying current velocity while holding buoyancy constant via kelp
652 density. Results are shown in Fig. A1.

653 The effective length predicted by our model compares well to the results from Eq. (A1) across
654 the entire range of P (Fig. A1a). The fractional error in predictions (Fig. A1b) is always below
655 10% for the range of P in our wave simulations ($0.01 < P < 4$). In addition to our neglect of
656 bending stiffness, differences could also originate from the error between the simulations in Luhar
657 and Nepf (2011) and their fitted equation, and also our inclusion of frond stretching. We note that

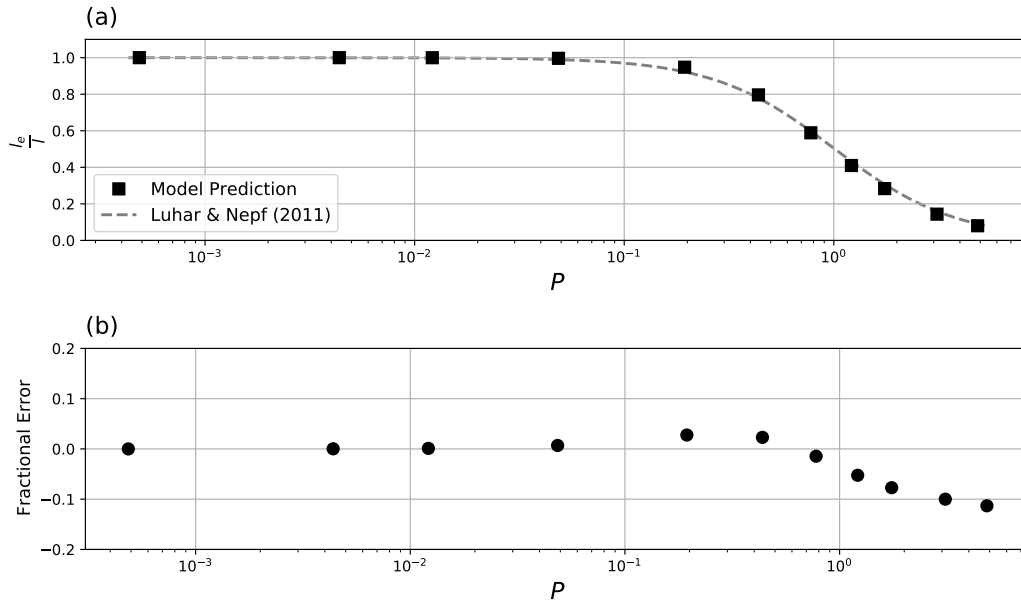


Figure A1. (a) Model predictions of effective length (black squares) compared to the model from Luhar and Nepf (2011) given by Eq. (A1) (dashed gray line). (b) Fractional error of present model predictions.

658 comparing Eq. (A1) including and neglecting Ca leads to errors of only up to 3% for the range
 659 of conditions used in our model. Therefore, despite the differences between blade response to
 660 a steady flow and our study of unsteady wave motion, we conclude that the errors incurred by ne-
 661 glecting bending stiffness in our numerical model are likely minor and would not impact the over-
 662 all conclusions of our study.

663 **Open Research Section**

664 The data required to reproduce the figures will be made available at a public repository prior to
 665 final publication.

666 **Acknowledgments**

667 The authors report no conflict of interest.

668 This work is supported by the ARPA-E MARINER Program (DE-AR0000920). JFM also grate-
 669 fully acknowledges support by the Sharon Fisher Endowment and the Norton Rodman Endow-
 670 ment (Undergraduate Research Scholars Program, UCLA Undergraduate Research Center – Sci-

671 ences), and the Queen’s Road Fellowship Program (with special thanks to its founder, Fritz De-
672 mopoulos).

673 Wave data were furnished by the Coastal Data Information Program (CDIP), Integrative Oceanog-
674 raphy Division, operated by the Scripps Institution of Oceanography, under the sponsorship of
675 the U.S. Army Corps of Engineers and the California Department of Parks and Recreation ([https://](https://doi.org/10.18437/C7WC72)
676 doi.org/10.18437/C7WC72).

677 **References**

678 Abbott, I. A., & Hollenberg, G. J. (1992). *Marine algae of california*. Stanford University
679 Press.

680 Dayton, P. K., Currie, V., Gerrodette, T., Keller, B. D., Rosenthal, R., & Tresca, D. V.
681 (1984). Patch dynamics and stability of some california kelp communities. *Ecological*
682 *Monographs*, 54(3), 253–289. <https://doi.org/10.2307/1942498>

683 Dean, R. G., & Dalrymple, R. A. (1991). *Water wave mechanics for engineers and scientists*
684 (Vol. 2). World Scientific Publishing Company. <https://doi.org/10.1142/1232>

685 Denny, M. W., Gaylord, B. P., & Cowen, E. A. (1997). Flow and flexibility ii. the roles of
686 size and shape in determining wave forces on the bull kelp *nereocystis luetkeana*. *Journal*
687 *of Experimental Biology*, 200(24), 3165–3183. [https://doi.org/10.1242/jeb.200.24](https://doi.org/10.1242/jeb.200.24.3165)
688 .3165

689 Eger, A. M., Marzinelli, E. M., Beas-Luna, R., Blain, C. O., Blamey, L. K., Byrnes, J. E., . . .
690 others (2023). The value of ecosystem services in global marine kelp forests. *Nature*
691 *Communications*, 14(1), 1894. <https://doi.org/10.1038/s41467-023-37385-0>

692 Elwany, M. H. S., O’Reilly, W. C., Guza, R. T., & Flick, R. E. (1995). Effects of south-
693 ern california kelp beds on waves. *Journal of Waterway, Port, Coastal, and Ocean En-*
694 *gineering*, 121(2), 143–150. [https://doi.org/10.1061/\(ASCE\)0733-950X\(1995\)121:](https://doi.org/10.1061/(ASCE)0733-950X(1995)121:2(143))
695 2(143)

696 Frieder, C. A., Yan, C., Chamecki, M., Dauhajre, D., McWilliams, J. C., Infante, J., . . .
697 Davis, K. A. (2022). A macroalgal cultivation modeling system (macmods): evaluat-
698 ing the role of physical-biological coupling on nutrients and farm yield. *Frontiers in*
699 *Marine Science*, 9. <https://doi.org/10.3389/fmars.2022.752951>

700 Froehlich, H. E., Afflerbach, J. C., Frazier, M., & Halpern, B. S. (2019). Blue growth po-
701 tential to mitigate climate change through seaweed offsetting. *Current Biology*, 29(18),
702 3087–3093. <https://doi.org/10.1016/j.cub.2019.07.041>

- 703 Gao, G., Gao, L., Jiang, M., Jian, A., & He, L. (2021). The potential of seaweed cultivation
704 to achieve carbon neutrality and mitigate deoxygenation and eutrophication. *Environ-*
705 *mental Research Letters*, *17*(1), 014018. <https://doi.org/10.1088/1748-9326/ac3fd9>
- 706 Gaylord, B., Denny, M. W., & Koehl, M. A. (2003). Modulation of wave forces on kelp
707 canopies by alongshore currents. *Limnology and Oceanography*, *48*(2), 860–871.
708 <https://doi.org/10.4319/lo.2003.48.2.0860>
- 709 Gaylord, B., Rosman, J. H., Reed, D. C., Koseff, J. R., Fram, J., MacIntyre, S., . . . others
710 (2007). Spatial patterns of flow and their modification within and around a giant kelp
711 forest. *Limnology and Oceanography*, *52*(5), 1838–1852. [https://doi.org/10.4319/](https://doi.org/10.4319/lo.2007.52.5.1838)
712 [lo.2007.52.5.1838](https://doi.org/10.4319/lo.2007.52.5.1838)
- 713 Henderson, S. M. (2019). Motion of buoyant, flexible aquatic vegetation under waves: sim-
714 ple theoretical models and parameterization of wave dissipation. *Coastal Engineering*,
715 *152*, 103497. <https://doi.org/10.1016/j.coastaleng.2019.04.009>
- 716 Hoegh-Guldberg, O., Lovelock, C., Caldeira, K., Howard, J., Chopin, T., & Gaines, S.
717 (2019). The ocean as a solution to climate change: five opportunities for action.
- 718 Jackson, G. A., & Winant, C. D. (1983). Effect of a kelp forest on coastal currents. *Continen-*
719 *tal Shelf Research*, *2*(1), 75–80. [https://doi.org/10.1016/0278-4343\(83\)90023-7](https://doi.org/10.1016/0278-4343(83)90023-7)
- 720 Johnson, A. S., & Koehl, M. A. R. (1994). Maintenance of dynamic strain similarity and
721 environmental stress factor in different flow habitats: thallus allometry and mate-
722 rial properties of a giant kelp. *Journal of Experimental Biology*, *195*(1), 381–410.
723 <https://doi.org/10.1242/jeb.195.1.381>
- 724 Journee, J., & Massie, W. (2000). *Offshore hydromechanics* (Vol. 1). CITG Section Hy-
725 draulic Engineering.
- 726 Kain, J. M., & Dawes, C. (1987). Useful european seaweeds: past hopes and present cultiva-
727 tion. *Hydrobiologia*, *151*, 173–181. <https://doi.org/10.1007/BF00046124>
- 728 Keulegan, G. H., & Carpenter, L. H. (1956). *Forces on cylinders and plates in an oscillating*
729 *fluid*. National Bureau of Standards.
- 730 Lei, J., & Nepf, H. M. (2019). Wave damping by flexible vegetation: Connecting individual
731 blade dynamics to the meadow scale. *Coastal Engineering*, *147*, 138–148. [https://doi](https://doi.org/10.1016/j.coastaleng.2019.01.008)
732 [.org/10.1016/j.coastaleng.2019.01.008](https://doi.org/10.1016/j.coastaleng.2019.01.008)
- 733 Luhar, M., & Nepf, H. M. (2011). Flow-induced reconfiguration of buoyant and flexible
734 aquatic vegetation. *Limnology and Oceanography*, *56*(6), 2003–2017. [https://doi.org/](https://doi.org/10.4319/lo.2011.56.6.2003)
735 [10.4319/lo.2011.56.6.2003](https://doi.org/10.4319/lo.2011.56.6.2003)

- 736 Luhar, M., & Nepf, H. M. (2016). Wave-induced dynamics of flexible blades. *Journal of*
 737 *Fluids and Structures*, *61*, 20–41. <https://doi.org/10.1016/j.jfluidstructs.2015.11.007>
- 738 Marjoribanks, T. I., Hardy, R. J., Lane, S. N., & Parsons, D. R. (2014). High-resolution
 739 numerical modelling of flow—vegetation interactions. *Journal of Hydraulic Research*,
 740 *52*(6), 775–793. <https://doi.org/10.1080/00221686.2014.948502>
- 741 Milledge, J. J., Smith, B., Dyer, P. W., & Harvey, P. (2014). Macroalgae-derived biofuel: a
 742 review of methods of energy extraction from seaweed biomass. *Energies*, *7*(11), 7194–
 743 7222. <https://doi.org/10.3390/en7117194>
- 744 Monismith, S., Alnajjar, M., Daly, M., Valle-Levinson, A., Juarez, B., Fagundes, M., . . .
 745 Woodson, C. B. (2022). Kelp forest drag coefficients derived from tidal flow data. *Es-*
 746 *tuaries and Coasts*, *45*(8), 2492–2503. <https://doi.org/10.1007/s12237-022-01098-2>
- 747 Mullarney, J. C., & Henderson, S. M. (2010). Wave-forced motion of submerged single-stem
 748 vegetation. *Journal of Geophysical Research: Oceans*, *115*(C12). [https://doi.org/10](https://doi.org/10.1029/2010JC006448)
 749 [.1029/2010JC006448](https://doi.org/10.1029/2010JC006448)
- 750 Mullarney, J. C., & Pilditch, C. A. (2017). The differential response of kelp to swell and in-
 751 fragravity wave motion. *Limnology and Oceanography*, *62*(6), 2524–2537. [https://doi](https://doi.org/10.1002/lno.10587)
 752 [.org/10.1002/lno.10587](https://doi.org/10.1002/lno.10587)
- 753 Nikora, V., Goring, D., & Biggs, B. (1998). A simple model of stream periphyton-flow inter-
 754 actions. *Oikos*, *81*, 607–611. <https://doi.org/10.2307/3546782>
- 755 Peteiro, C. (2018). Alginate production from marine macroalgae, with emphasis on kelp
 756 farming. *Alginates and Their Biomedical Applications*, *11*, 27–66. [https://doi.org/10](https://doi.org/10.1007/978-981-10-6910-9_2)
 757 [.1007/978-981-10-6910-9_2](https://doi.org/10.1007/978-981-10-6910-9_2)
- 758 Razmi, A. M., Chamecki, M., & Nepf, H. M. (2020). Efficient numerical representation
 759 of the impacts of flexible plant reconfiguration on canopy posture and hydrodynamic
 760 drag. *Journal of Hydraulic Research*, *58*(5), 755–766. [https://doi.org/10.1080/](https://doi.org/10.1080/00221686.2019.1671511)
 761 [00221686.2019.1671511](https://doi.org/10.1080/00221686.2019.1671511)
- 762 Rosman, J. H., Denny, M. W., Zeller, R. B., Monismith, S. G., & Koseff, J. R. (2013). Inter-
 763 action of waves and currents with kelp forests (*macrocystis pyrifera*): Insights from a
 764 dynamically scaled laboratory model. *Limnology and Oceanography*, *58*(3), 790–802.
 765 <https://doi.org/10.4319/lo.2013.58.3.0790>
- 766 Sarpkaya, T., & O’Keefe, J. L. (1996). Oscillating flow about two and three-dimensional
 767 bilge keels. *Journal of Offshore Mechanics and Arctic Engineering*, *118*(1), 1–6.
 768 <https://doi.org/10.1115/1.2828796>

- 769 Schiel, D. R., & Foster, M. S. (2015). *The biology and ecology of giant kelp forests*. Univer-
770 sity of California Press.
- 771 Seymour, R., Tegner, M., Dayton, P., & Parnell, P. (1989). Storm wave induced mortality
772 of giant kelp, *Macrocystis pyrifera*, in southern California. *Estuarine, Coastal and Shelf*
773 *Science*, 28(3), 277–292. [https://doi.org/10.1016/0272-7714\(89\)90018-8](https://doi.org/10.1016/0272-7714(89)90018-8)
- 774 Thornton, T. F. (2015). The ideology and practice of Pacific herring cultivation among the
775 Tlingit and Haida. *Human Ecology*, 43, 213–223. <https://doi.org/10.1007/s10745-015-9736-2>
- 776
- 777 Utter, B. D., & Denny, M. W. (1996). Wave-induced forces on the giant kelp *Macrocystis*
778 *pyrifera* (Agardh): field test of a computational model. *Journal of Experimental Biol-*
779 *ogy*, 199(12), 2645–2654. <https://doi.org/10.1242/jeb.199.12.2645>
- 780 Vogel, S. (1984). Drag and flexibility in sessile organisms. *American Zoologist*, 24(1), 37–
781 44. <https://doi.org/10.1093/icb/24.1.37>
- 782 Zeller, R. B., Weitzman, J. S., Abbett, M. E., Zarama, F. J., Fringer, O. B., & Koseff, J. R.
783 (2014). Improved parameterization of seagrass blade dynamics and wave attenuation
784 based on numerical and laboratory experiments. *Limnology and Oceanography*, 59(1),
785 251–266. <https://doi.org/10.4319/lo.2014.59.1.0251>
- 786 Zhu, L., Zou, Q.-P., Huguenard, K., & Fredriksson, D. W. (2020). Mechanisms for the
787 asymmetric motion of submerged aquatic vegetation in waves: a consistent-mass cable
788 model. *Journal of Geophysical Research: Oceans*, 125(2). <https://doi.org/10.1029/2019JC015517>
789